7

Cesium Lead Halide Perovskite ($CsPbX_3$) Nanocrystal Composites with Graphitic Carbon Nitride ($g\text{-}C_3N_4$) and Metal Oxide for Photo/-photoelectrocatalytic Applications

The work described in this chapter has been carried out at University of Alberta (UoA) under the SERB-UoA, Overseas Visiting Doctoral Fellowship (OVDF) Programme.

Perovskites are a class of compound having the chemical formula ABO_3, discovered in the Ural Mountains of Russia and named after the mineralogist Lev Perovski. These compounds exhibit wide variety of physical and chemical properties and are used importantly in numerous technological applications. It has twelve co-ordinated cations at 'A' site and smaller sized six co-ordinated cations at 'B' site. Variations in structure could be due to distortions of the octahedra, replacements of cations in the octahedral and tilting of octahedra. A very interesting class of perovskite called halide perovskite with general formula ABX_3 where the A site is replaced by a monovalent organic cations such as methylammonium cation $(CH_3NH_3)^+$ and formamidinium cation $(NH_2CH{=}NH_2)^+$ are gaining popularity because of their small bandgap (1.5 to 2.3 eV) and long charge carrier transport. These are used as active light absorbers in solar cells achieving an efficiency of over >20%. Compared to these Halide Organic-Inorganic Perovskites (HOIPs), all inorganic perovskites (AIP) provide an extensive range of material for better investigation and comparative stability. One example is $CsPbX_3$ where Cs^+ replaces the organic cation, discovered in 1958. Interestingly, AIP quantum dots exhibits compositional and size-based bandgap engineering whereby the optical band gap can be tuned according to the types of ions present. Furthermore, caesium-based halide perovskite quantum dots also exhibit high quantum yield, short radiative lifetimes and narrow emission line widths. Thus, these are mostly used in low threshold lasers, LEDs and solar cells. However, the application of these perovskite materials in photocatalysis is least studied due to the stability issue. Stabilization of perovskite quantum dots using inert surface passivating materials such as silica or long alkyl chains compromise the photocatalytic performance.

In this study, above mention $CsPbBr_3$ quantum dots instability issue was overcome by encasing quantum dots in a very thin film of metal oxides (Ti, Sn, Mo and Ta). $CsPbBr_3$ quantum dots were synthesized by a hot injection method followed by the coating of metal oxide film by slow hydrolysis of metal propoxides. Additionally, 2D graphenic semiconductor called $g\text{-}C_3N_4$ was also incorporated in and on $CsPbBr_3$ perovskite quantum dots. The prepared materials demonstrated excellent stability and used for photoelectrochemical water splitting and CO_2 reduction applications.

7.1 Experimental techniques

7.1.1. Preparation of Cesium oleate

Cesium oleate precursor was synthesized by mixing 36 wt % Cs_2CO_3/OA in 1-octadecene. The reaction mixture was heated in a three-neck bottom flask under an inert atmosphere at 120 °C for 1h followed by 150 °C until the complete dissolution of Cs_2CO_3 precursor. Typically, 814 mg of Cs_2CO_3, 2.5 mL OA and 10 mL ODE were mixed to form Cs-oleate solution which can be stored at room temperature for further use by re-heating at 150 °C.

7.1.2. Preparation of cesium lead halide quantum dots ($CsPbBr_3$)

A typical hot injection method was adopted for the synthesis of $CsPbBr_3$ nanocrystals in an inert N_2 atmosphere in a two-neck flask with 138 mg $PbBr_2$ in 10 mL ODE under continuous stirring and heating at 120 °C for 1 h. After which, 1 mL each of OA and OAm were injected in the reaction system following which the temperature is raised to 180 °C and rapidly 1 mL of the Cs-oleate solution was injected after which the solution turns turbid and fluorescent green colour. 5s into the reaction, the system is then suddenly cooled using an ice water bath. Subsequently, the as-prepared material is washed with hexane three times in a centrifuge at 8000 rpm. The collected precipitate is kept in a hexane suspension for further use. For the synthesis of composites of monolayer sheets of graphitic carbon nitride and $CsPbBr_3$ (GCN-$CsPbBr_3$), monolayer graphitic carbon nitride dispersed in ODE by sonicating for an hour The ODE dispersed CN sheets were added to $PbBr_2$ in ODE solution and heated at 120 °C for 1 h with continuous stirring under N_2 atmosphere. Other steps were similar to $CsPbBr_3$ quantum dots synthesis. For the process of encapsulation with various oxides of metal such as Ti, Ta, Mo and Sn, respective precursor materials were added into the solution of $CsPbBr_3$ solution at 70 °C under ambient atmosphere for a time interval of 30 mins. The encapsulated colloidal solution was then correspondingly named.

7.2 Results and discussion

A solution process of synthesis was adopted for the synthesis of luminescent AIPs ($CsPbBr_3$). In this protocol, the hot injection method was used which required the use of an external source of energy to provide activation energy to form $CsrPbBr_3$ nanocrystals. The solution process is advantageous as it results in highly crystalline nanomaterials.

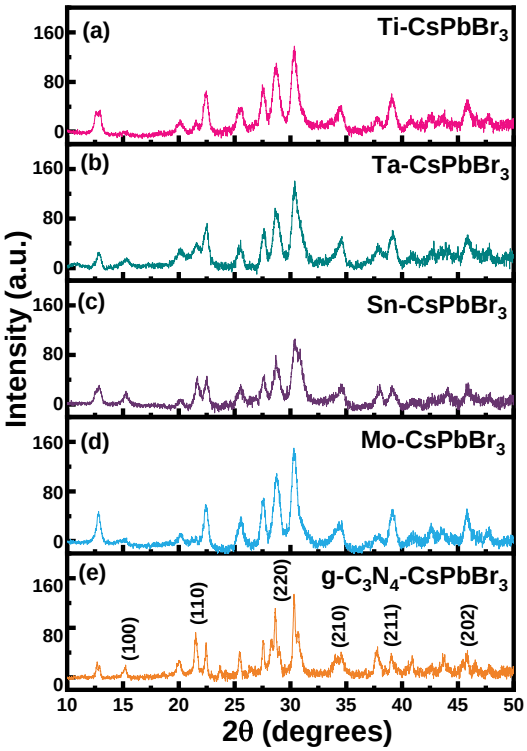

Figure 7.1: X-ray diffraction pattern of the $CsPbBr_3$ composites with Ti, Ta, Sn, Mo oxide and g-C_3N_4.

The XRD pattern of the different metal oxides and graphitic carbon nitride encased $CsPbBr_3$ nanocrystals are given in Figure 7.1. As it can be observed that all the XRD patterns towel matched with the reported literature (Swarnkar, Chulliyil et al. 2015) corresponded to an orthorhombic phase of $CsPbBr_3$. Additionally, the diffraction peaks were broad in nature which might indicate small particle size. Furthermore, it can also be seen that the incorporation of graphitic carbon nitride (GCN) and other metal oxides did not significantly change the crystal structure of the $CsPbBr_3$ crystal structure. Peaks of the metal oxide and GCN were not observed

in the XRD pattern that might be due to their amorphous nature. The photoluminescence (PL) spectra of the synthesized $CsPbBr_3$ along with the different composites are shown in Figure 7.2. The $CsPbBr_3$ nanocrystals displayed a bright PL emission in between 480-520 nm with a peak maximum at 510 nm. The PL intensity was drastically reduced for a few of the synthesized material namely, Ta-$CsPbBr_3$, GCN-$CsPbBr_3$ and Ti-$CsPbBr_3$ which was attributed due to decreased charge recombination in these composites showing quenching effect. Additionally, the blue shift for Ta-$CsPbBr_3$ and Sn-$CsPbBr_3$ and redshift for GCN-$CsPbBr_3$ and Ti-$CsPbBr_3$ might be due to the interaction of metal oxide with $CsPbBr_3$nanocrystals and changed domain sizes respectively (Xu, Wang et al. 2018). Interestingly the decreased PL intensity also suggests non-radiative pathway of electron and hole recombination. TiO_2 has been extensively investigated photocatalyst and possesses a proper band alignment with the $CsPbBr_3$ nanocrystals and can accept the injected electrons from the AIPs. Similar might be the case for GCN-$CsPbBr_3$ and other composites and it will be interesting to investigate its performance in device application. The UV-vis spectra of $CsPbBr_3$ and their composites are given Figure 7.2b. The absorption band edge of all the synthesized $CsPbBr_3$ nanocrystal and their composites were found to be around 520-530 nm demonstrating $CsPbBr_3$ nanocrystal mainly contributes in absorption spectra.

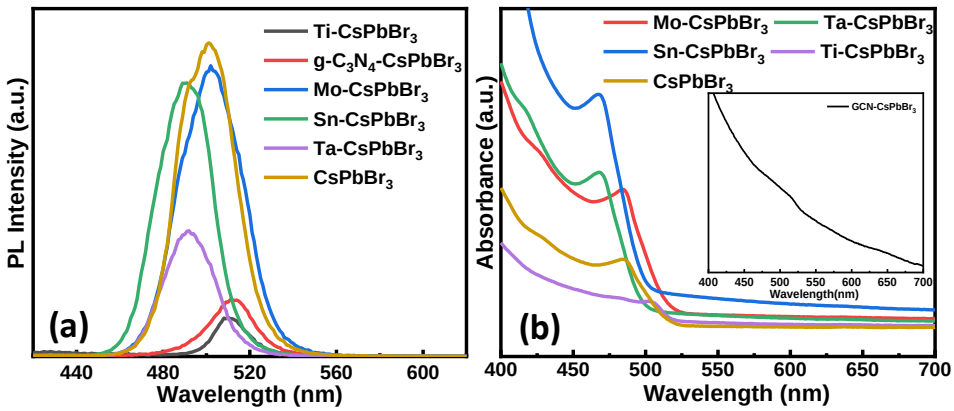

Figure 7.2: PL spectra (a) and UV-vis spectra (b) of the synthesized different $CsPbBr_3$ composites. Inset (b) shows the band adsorption edge of GCN-$CsPbBr_3$ at 520 nm.

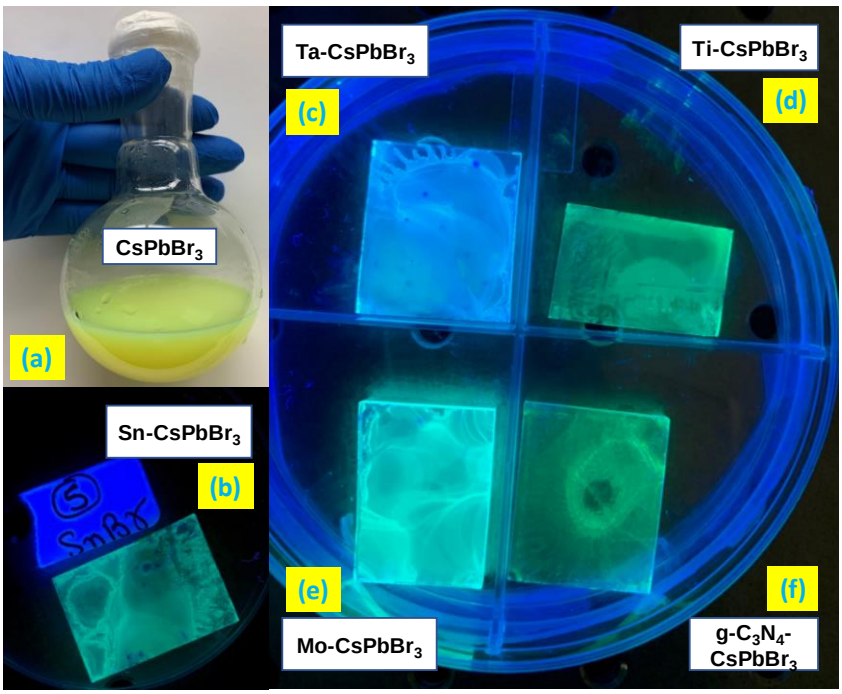

Figure 7.3: Photographic images of pristine $CsPbBr_3$ (a) under day light and under UV light (λ = 365 nm) of Sn-$CsPbBr_3$ (b), Ta-$CsPbBr_3$ (c), Ti-$CsPbBr_3$ (d), Mo-$CsPbBr_3$ (e) and GCN-$CsPbBr_3$ (f) deposited on glass.

Figure 7.3 shows the photographic image of the synthesized $CsPbBr_3$ nanocrystals and the luminescent images as observed under 365 nm UV light for Sn-$CsPbBr_3$, Ta-$CsPbBr_3$, Ti-$CsPbBr_3$, Mo-$CsPbBr_3$ and GCN-$CsPbBr_3$ respectively.

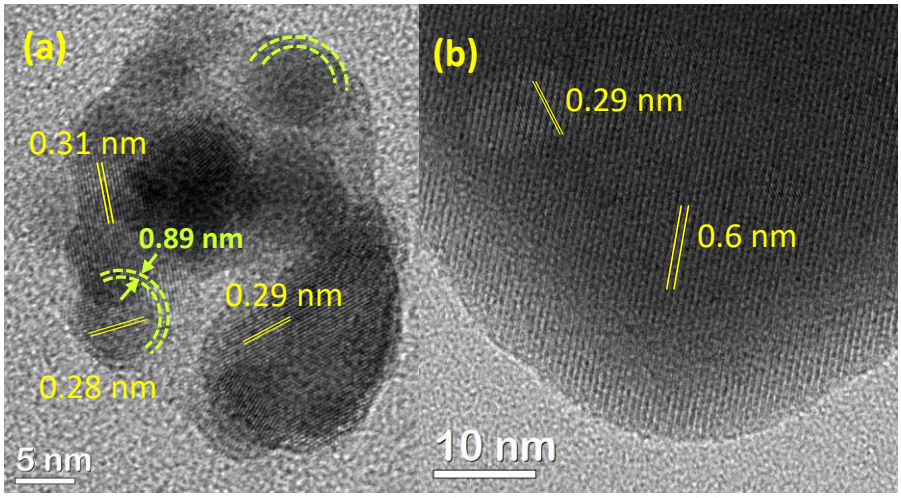

Figure 7.4: High resolution TEM images of Mo-$CsPbBr_3$ (a) and GCN-$CsPbBr_3$ (b) showing lattice fringes and d-spacing

The precursors were added to encapsulate and passivate the surface of the unstable perovskite nanocrystals. For the metal oxides, a temperature of about 70 °C is enough to do hydrolysis of the precursors over the unstable $CsPbBr_3$ providing it better stability. The encapsulated coating of the metal precursors can be observed in the TEM image for Mo-$CsPbBr_3$ (Figure 7.4a). As indicated in the figure the thickness of the shell was found to be approximately 0.85 nm. Additionally, lattice planes were visible and the observed d-spacing of 0.28 nm corresponds to (220) plane of the $CsPbBr_3$ crystal indicating the presence of high crystallinity of the synthesized materials (Xu, Yang et al. 2017). The obtained results were in accordance with XRD results (Figure 7.1). The HRTEM image of GCN-$CsPbBr_3$ nanocrystals displayed a d-spacing of 0.29 nm which corresponds to that of $CsPbBr_3$ (Figure 7.4b). A *d*-spacing of 0.6 nm was corroborated to the Moire fringes originating from superimposition mismatch of inter layer planes of graphitic carbon nitride sheets (Wang, Hao et al. 2017).

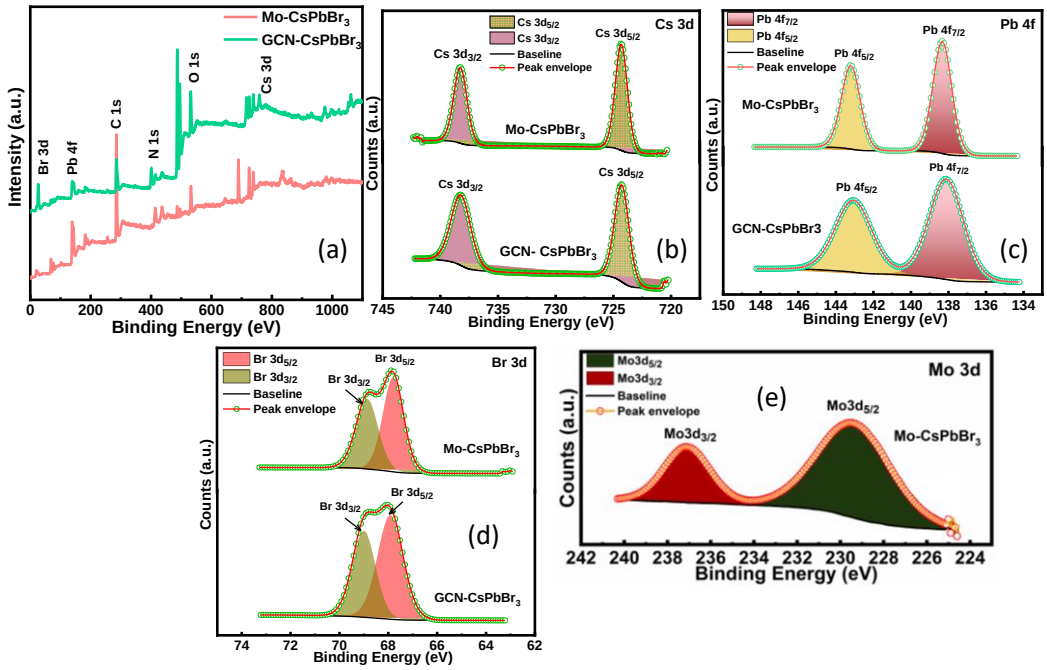

Figure 7.5: Survey scan (a) and High resolution XPS spectra of Mo-$CsPbBr_3$ and GCN-$CsPbBr_3$ in Cs 3d (b), Pb 4f (c), Br 3d (d) and Mo 3d (e) region.

X-ray photoelectron spectroscopy was further performed for the encapsulated Mo-$CsPbBr_3$ and GCN-$CsPbBr_3$ composite to validate the presence of various elements using surface elemental analysis. The survey scan Mo-$CsPbBr_3$ and GCN-$CsPbBr_3$ depicted in Figure 7.5a reveals all the constituting elements present in materials suggesting metal and the GCN remain undoped. The high resolution XPS spectra Mo- and GCN – $CsPbBr_3$ in Cs 3d region shows two peaks at binding energies at 738.2 eV and 724.3 eV corresponding to Cs $3d_{5/2}$ and Cs $3d_{3/2}$ peak components of Cs present in +1 oxidation state (see Figure 7.5b). The XR-XPS spectra in Pb 4f region for both the perovskites samples exhibited two peaks components located at 143.2 eV and 138.32 eV assigned to Pb $4f_{5/2}$ and Pb $4f_{7/2}$ confirming the presence of Pb^{2+} cations as shown in Figure 7.5c (Liu, Zhong et al. 2017). There is no observed relative shift in the peaks verifying well preserved structure. In Figure 7.5d, two well resolved Br 3d peaks in both perovskite samples centered at 68.02 eV and 69.02 eV corroborated to the Br $3d_{5/2}$ and Br $3d_{3/2}$. A minor shift in the case of GCN based perovskite to a lower binding energy at 67.92 eV might be due to the formation of C-N-Br bonds (Ou, Tu et al. 2018).

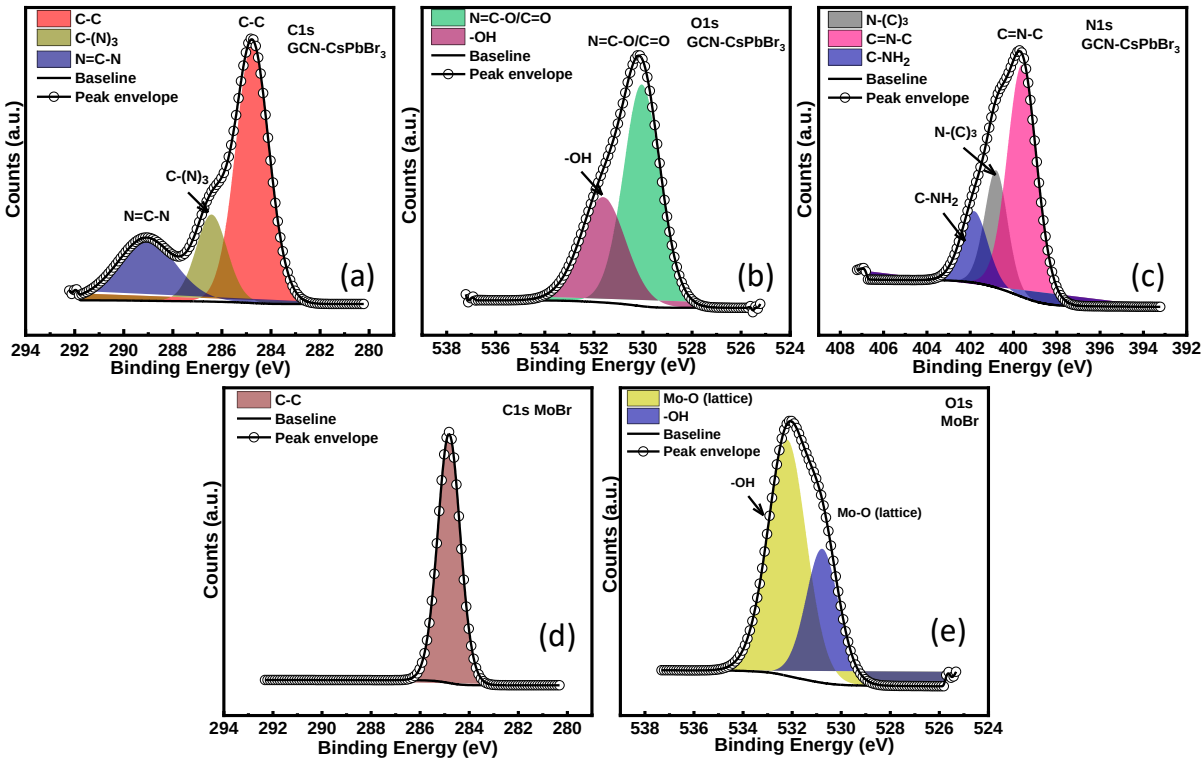

Figure 7.6: High resolution XPS spectra of GCN-$CsPbBr_3$ in C 1s (a), O 1s (b) and N 1s (c) region and Mo-$CsPbBr_3$ in C 1s (d) and O 1s (e) region.

The C 1s spectrum of GCN based perovskite can be resolved into three peak components which can be attributed to triazine coordination of N=C-N at 289.2 eV, C-$(N)_3$ at 286.4 eV present on heptazine nucleus and the peak centered at 284.8 eV was attributed to the presence of turbostratic adventitious carbons present in surface adsorbed residual long-chain alkyl chain (Figure 7.6). However, it is interesting to note that the Mo-$CsPbBr_3$ displayed a single peak at around 284.8 eV in Figure 7.6d which can be due to the presence of adventitious carbon. Both metal encapsulated perovskite (Figure 7.6b) and GCN composite perovskite (Figure 7.6d) show two resolved O1s peaks located at 530.5 eV and 532.4 eV attributed to the C=O and hydroxyl groups oxygen respectively. The relatively intense peak at 530.5 eV for GCN-$CsPbBr_3$ might be due to the contribution from the uncondensed N=C-O and C=O groups at the edge of graphitic carbon nitride framework. Additionally, the N 1s peak for GCN-$CsPbBr_3$ can be deconvoluted into three constituent peaks at 401.7 eV due to the presence of amino groups such as C-NH_2 while the peak at around 400.82 eV and 399.62 eV were originated due to the presence of sp^2

hybridized tertiary nitrogen groups (N-(C)$_3$) and secondary (C=N-C) nitrogen atoms of heptazine nucleus (Ou, Tu et al. 2018).

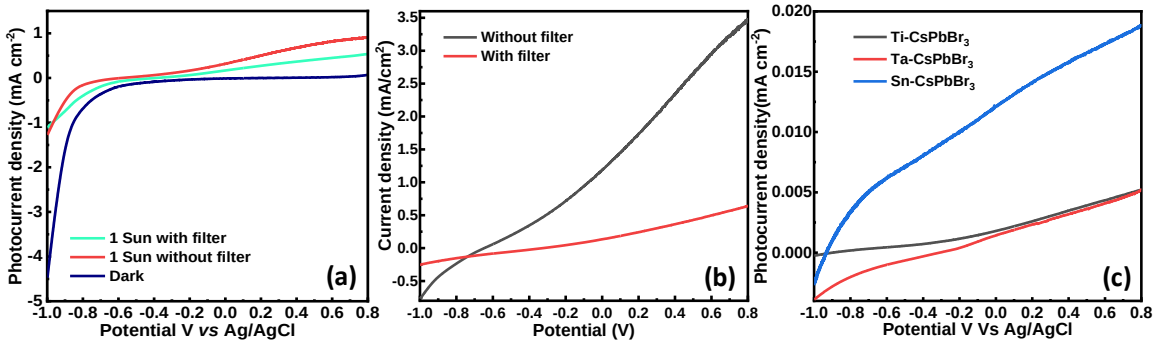

Figure 7.7: Linear sweep voltammetry (LSV) under AM1.5 G solar simulated light with and without 420 nm UV cut-off filter for (a) GCN-CsPbBr$_3$ and (b) Mo-CsPbBr$_3$ and (c) LSV of Ti-CsPbBr$_3$, Ta-CsPbBr$_3$ and Sn-CsPbBr$_3$ without UV filter.

In order to evaluate the performance of the synthesized materials, photoelectrochemical testing utilizing these materials was performed. An FTOs spin-coated with these materials was subjected as photoanode in a three-electrode system with Pt as counter electrode and Ag/AgCl as the reference electrode under a solar simulated AM1.5 G irradiation and 0.1 M Na_2SO_4 electrolyte solution. To validate visible light induced water splitting a 420 nm cut off filter was employed to filter out wavelength shorter than 420 nm. LSV measurement (Figure 7.7) was performed for all the synthesized materials from a scan range of -0.1 V to +0.1 V vs Ag/AgCl. GCN-CsPbBr$_3$ showed a photocurrent density of 0.9 mA/cm^2 without applying filter which decreases to 0.5 mA/cm^2 in the presence of a UV cut-off filter. For Mo encapsulated CsPbBr$_3$ perovskite, the photocurrent density without a filter was relatively higher with 3.5 mA/cm^2 but it sharply decreases in the presence of filter to about 0.5 mA/cm^2. As expected, due to the large bandgap of MoO_3 shell, the contribution of UV light was maximum in the case of Mo-CsPbBr$_3$. Additionally, for the Ta-CsPbBr$_3$, Ti-CsPbBr$_3$, and Sn-CsPbBr$_3$ in the absence of UV cut-off filter the observed photocurrent density was substantially lower and hence these two materials viz. Mo-CsPbBr$_3$ and GCN-CsPbBr$_3$ will be studied in detail.

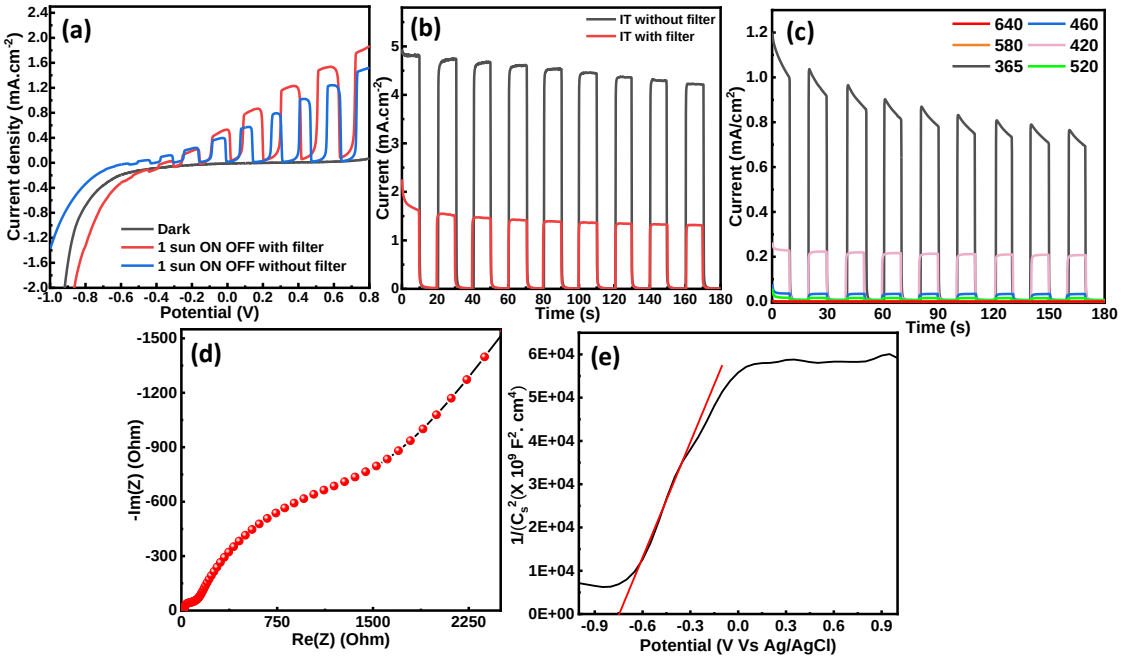

Figure 7.8: Photoelectrochemical study of GCN-CsPbBr$_3$. Current density vs applied voltage curve during an ON-OFF light cycle (a), Light On-OFF amperometric i-t curve under AM1.5G solar simulated light with and without 420 nm cut-off filter (b), Amperometric *Ii-t* curve at +0.6 V applied bias when exposed to LEDs of different wavelength at 365, 420, 460, 580 and 640 nm (c), EIS Nyquist plot (d) and Mott-Schottky (e).

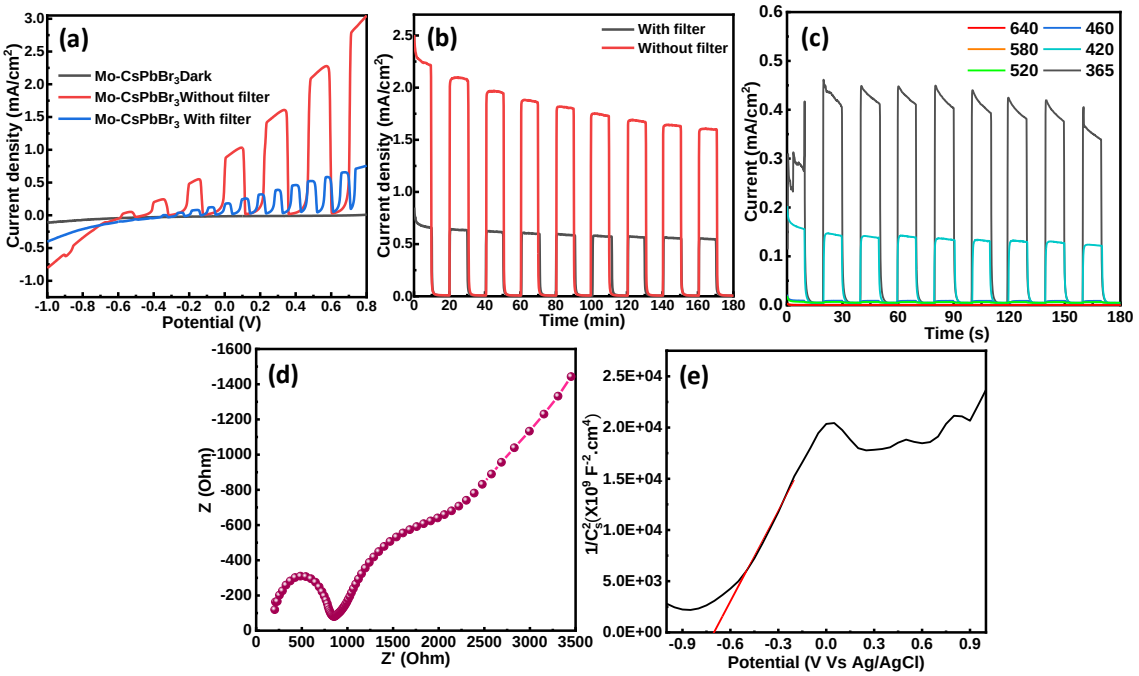

Figure 7.9: Photoelectrochemical study of Mo-CsPbBr$_3$. Current density Vs voltage curve during an ON-OFF light cycle (a), Light On-OFF amperometric *i-t* curve under AM1.5G solar simulated light with and without 420 nm filter cut-off of (b), Amperometric i-t curve at +0.6 V applied bias when exposed to LEDs of different wavelength at 365, 420, 460, 580 and 640 nm (c), EIS Nyquist plot (d) and Mott-Schottky (e).

When light is exposed to the active surface area, the electron-hole pairs are generated which gets separated and migrated to the electrode surface under the influence of the applied external bias. The photoelectrochemical behavior for both the encapsulated and composite perovskites are shown in Figure 7.8 and Figure 7.9 at AM 1.5. The photocurrent density with and without cut-off filter reveals consistency for GCN-CsPbBr$_3$ (Figure 7.8a) unlike for the Mo-CsPbBr$_3$ (Figure 7.9a) that exhibits high photocurrent without the cut-off filter and drastically reduces with filter. Photocurrent transient measurements (Figure 7.8b and 7.9b) were further employed which show the constant response of compared to Mo-perovskite. Similar results were observed employing LEDS having different wavelength – 365, 420, 460, 520, 580 and 640 nm (Figure 7.8c and 7.9c). The carrier transport parameters such as charge transfer resistance, charge transport resistance etc. were measured using the Electrochemical Impedance Spectroscopy (EIS) techniques. EIS Nyquist plot is shown in Figure 7.8d and 7.9d demonstrates a decrease in charge transfer resistance in the GCN-CsPbBr$_3$ as evident from the small semi-circular arc in the high-frequency region. Additionally, the flat band potential was calculated by using the Mott Schottky plot and the GCN-perovskite composite showed a larger negative shift compared to the Mo protected perovskite.

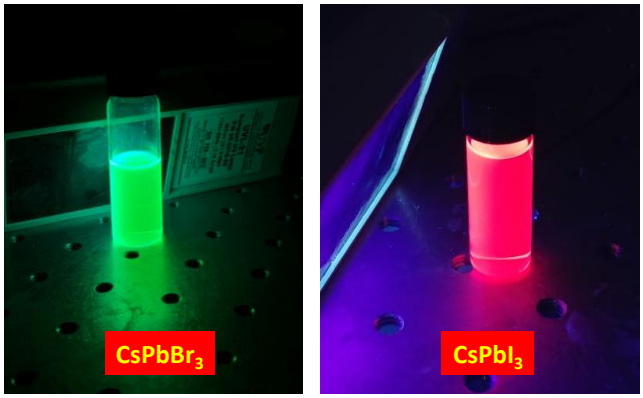

Figure 7.10: Photographic image of all inorganic perovskite CsPbBr$_3$ and CsPbI$_3$ demonstrating the change in photoluminescence (green to red) by changing the constituting anion.

It is interesting to observe the tunability of the $CsPbX_3$ perovskites by changing the constituting anions of the perovskite. Figure 7.10 shows a sharp change in photoluminescence from green to red under a 365 nm UV lamp when the bromide ion in the $CsPbBr_3$ was replaced by I^- ion. This indicates that by changing the composition the wavelength tunability can be achieved.

7.3 Conclusion

In summary, a simple solution process using a hot injection method was adopted for preparing an All Inorganic Perovskites (AIPs), $CsPbBr_3$. However, the instability issues of this material under ambient atmosphere and in contact with moisture makes it disadvantageous for use in fabrication and device application. Therefore, to address this issue a protective covering using metal oxides namely Mo, Ta, Ti and Sn was used for encapsulating the $CsPbBr_3$ perovskite nanocrystals. Additionally, monolayer graphitic carbon nitride sheets were coupled to make a composite with the perovskite. The synthesized materials were characterized using various techniques such as XRD, TEM, XPS, UV and PL to analyze the changes and the properties after the encapsulation and formation of the composite. Furthermore, the synthesize materials were used for photoelectrochemical water splitting to study electronic properties such as generated photocurrent, behavior in light, charge transport resistance, etc. Finally, the compositional tuning of AIP is evidently observed by changing the anion part in the perovskite by replacing Br^- with I^- which is accompanied by a red luminescence.